Boundary-Layer Meteorol (2008) 127:273–292
DOI 10.1007/s10546-007-9254-x

ORIGINAL PAPER

A Modelling Study of Flux Imbalance and the Influence of Entrainment in the Convective Boundary Layer

Jianping Huang · Xuhui Lee · Edward G. Patton

Received: 25 July 2007 / Accepted: 27 November 2007 / Published online: 19 December 2007

Abstract It is frequently observed in field experiments that the eddy covariance heat fluxes are systematically underestimated as compared to the available energy. The flux imbalance problem is investigated using the NCAR's large-eddy simulation (LES) model imbedded with an online scheme to calculate Reynolds-averaged fluxes. A top–down and a bottom–up tracer are implemented into the LES model to quantify the influence of entrainment and bottom–up diffusion processes on flux imbalance. The results show that the flux imbalance follows a set of universal functions that capture the exponential decreasing dependence on u_*/w_*, where u_* and w_* are friction velocity and the convective velocity scale, respectively, and an elliptic relationship to z/z_i, where z_i is the mixing-layer height. The source location in the boundary layer is an important factor controlling the imbalance magnitude and its horizontal and vertical distributions. The flux imbalance of heat and the bottom–up tracer is tightly related to turbulent coherent structures, whereas for the top–down diffusion, such relations are weak to nonexistent. Our results are broadly consistent with previous studies on the flux imbalance problem, suggesting that the published results are robust and are not artefacts of numerical schemes.

Keywords Bottom–up tracer · Eddy covariance · Entrainment · Energy imbalance · Large-eddy simulation model · Top–down tracer

1 Introduction

Energy conservation is a fundamental law to both observational and modelling studies of land–atmosphere interactions. Eddy covariance (EC) is the most common method for measuring the vertical turbulent fluxes. The EC data provide a crucial means for evaluating

J. Huang (✉) · X. Lee
School of Forestry and Environmental Studies, Yale University, New Haven, CT, USA
e-mail: jianping.huang@yale.edu

E. G. Patton
National Center for Atmospheric Research, Boulder, CO, USA

land-surface process parameterization schemes in regional and global weather and climate models. It is well-known, however, that the turbulent heat fluxes as measured by the EC method do not add up to the available energy. Numerous experimental studies found that the sensible and latent heat fluxes are systematically underestimated, typically by 10–30%, as compared to the available energy (Lee and Black 1993; Mahrt 1998; Twine et al. 2000; Wilson et al. 2002). The flux imbalance problem is a serious contradiction to the energy conservation principle. A better understanding of the mechanisms of the imbalance continues to represent the most challenging aspect of the EC and modelling studies of land-surface processes.

So far, the imbalance problem has been attributed to either the uncertainties of observational conditions related to sites and instruments, or the influence of flow field and turbulent structures in the planetary boundary layer (PBL). Numerical fluid mechanic models are powerful tools in the investigation of the influence of the flow field and turbulent structures. For instance, Kanda et al. (2004) (referred to as K04 hereafter) used a parallelized large-eddy simulation (LES) model (PALM) (Raasch and Schröter 2001) to study the sensible heat flux imbalance problem. In the LES framework, imbalance is defined as the deviation of the Reynolds or temporally averaged heat flux at a grid point from the horizontally averaged total heat flux. They concluded that the existence of turbulent organized structures (TOS) is responsible for the flux imbalance. They also pointed out the dependence of the imbalance of heat flux on geostrophic wind and measurement height. Later, using the same LES model but with a finer spatial resolution, Steinfeld et al. (2007) (S07 hereafter) confirmed the findings of K04 and also investigated how surface heat flux and stable stratification affect the imbalance magnitude.

In this study, we revisit the flux imbalance problem using a modelling approach. Our research builds on the work of K04 and S07. Like K04 and S07, we also use a LES model—the LES model developed by the National Center for Atmospheric Research (NCAR) (Moeng 1984; Sullivan et al. 1996; Patton et al. 2005)—to simulate the flow and scalar concentration fields, and set up "virtual towers" in the model domain to mimic the EC observations. The first specific objective of the study is to verify that the previous results (e.g., K04 and S07) are not a model artifact. Although all LES models are based on the same fundamental governing equations, they differ in aspects of numerical schemes. For example, the NCAR's LES model uses the pseudospectral method and centered finite-differencing to calculate horizontal and vertical derivatives, respectively (Moeng 1984), whereas PALM employs the scheme proposed by Piacsek and Williams (1970) or the upstream-spline scheme (Purnell 1976) to approximate the advection term, and second-order finite differences to treat the diffusion terms (Raasch and Schröter 2001).

The second specific objective is to search for universal functions that describe the dependence of flux imbalance on driving variables such as friction velocity (u_*), measurement height (z), and the convective velocity scale (w_*). This is made possible by the extended parameter space through an online scheme embedded in the NCAR's LES. In the online mode, instead of writing the simulated fields into output files, the LES model "memorizes" the predicted instantaneous fields for all variables of interest at all grid points within the model domain and produces time averaged (Reynolds) statistics over a pre-specified period of simulation. Thus, the flux imbalance pattern can be investigated throughout the PBL. Although most of EC experiments are conducted in the surface layer near the ground, the imbalance problem in the middle and upper boundary layer is relevant to observations made on tall towers and aircraft (Mahrt 1998; Davis et al. 2003).

Our third specific objective is to investigate the influence of the entrainment process on the flux imbalance problem. While heat flux in the lower part of the PBL, the case studied

by K04 and S07, is dominated by diffusion from the bottom–up process, for scalars such as water vapor and carbon dioxide, entrainment at the PBL top plays an important role in their diffusion and transport in the convective boundary layer. Entrainment has been shown by Wyngaard and Brost (1984) to have a significant influence on the mean scalar mixing ratio profile in the convective PBL through the so-called "top–down" diffusion. In order to isolate the roles of both the top–down and the bottom–up diffusion on flux imbalance, two scalars, a top–down tracer (χ_t) and a bottom–up tracer (χ_b), in addition to sensible heat, are implemented in our LES simulations.

2 Temporal Versus Spatial Averaging

The theoretical background regarding the heat flux imbalance problem resulting from single-tower measurements has been described in detail by K04 and S07. A brief description is given here. Let us consider the imbalance problem for scalar φ. Let $\overline{\varphi}$ and $\langle\varphi\rangle$ denote its temporal and spatial averages, respectively, and φ' and φ'' denote its temporal and spatial fluctuations, respectively. Here the overbar represents the temporal averaging operation and $\langle\rangle$ the spatial averaging in the x–y cross-section. By definition, the temporal and spatial fluctuations of vertical velocity (w) and scalar (φ) can be expressed by

$$w' = w - \overline{w},\ \ \varphi' = \varphi - \overline{\varphi}, \tag{1a}$$

$$w'' = w - \langle w\rangle\,,\ \ \varphi'' = \varphi - \langle\varphi\rangle\,. \tag{1b}$$

Accordingly, the temporal or Reynolds and spatial covariances are written as

$$\overline{w'\varphi'} = \overline{w\varphi} - \overline{w}\,\overline{\varphi}, \tag{2a}$$

$$\left\langle w''\varphi''\right\rangle = \langle w\varphi\rangle - \langle w\rangle\,\langle\varphi\rangle\,. \tag{2b}$$

In Eq. 2a, $\overline{w'\varphi'}$ represents the vertical flux of scalar φ as measured by the EC method at a single tower. Here φ represents mixing ratio, except for temperature. Therefore the Reynolds flux in Eq. 2a does not need density corrections (Leuning 2004). In Eq. 2b, the spatial covariance $\left\langle w''\varphi''\right\rangle$ represents the vertical flux of scalar φ attributed to the motion of resolved eddies. While the mean vertical velocity is not vanishing (Webb et al. 1980), it is extremely small as compared to the turbulent fluctuations. Typically, $\langle w\rangle$ ranges from 0 to 0.1 m s^{-1}, while w'' has a magnitude of $\pm$3–4 m s^{-1}. Furthermore, the averaging period (1-h in this study) is much shorter than the time scale of variations in the external large-scale forcing. Thus, the assumption of $\langle w\rangle = 0$ is satisfied in our simulations, and Eq. 2b is reduced to

$$\left\langle w''\varphi''\right\rangle = \langle w\varphi\rangle\,. \tag{2c}$$

Next we perform the spatial averaging on Eq. 2a and Reynolds averaging on Eq. 2c to obtain

$$\left\langle\overline{w'\varphi'}\right\rangle = \langle\overline{w\varphi}\rangle - \langle\overline{w}\,\overline{\varphi}\rangle\,, \tag{3a}$$

$$\overline{\langle w''\varphi''\rangle} = \overline{\langle w\varphi\rangle}, \tag{3b}$$

where $\overline{\langle w\varphi\rangle}$ is equal to $\langle\overline{w\varphi}\rangle$.

According to K04, in the absence of mean vertical motion in the PBL ($\langle w \rangle = 0$), the scalar flux imbalance (I_φ) at any given grid point in the model domain is written

$$I_\varphi = \frac{\overline{w'\varphi'} - \overline{\langle w''\varphi'' \rangle}}{\overline{\langle w''\varphi'' \rangle}} \tag{4a}$$

and the flux imbalance averaged over the x–y cross-section is

$$\langle I_\varphi \rangle = \frac{\left\langle \overline{w'\varphi'} \right\rangle - \overline{\langle w''\varphi'' \rangle}}{\overline{\langle w''\varphi'' \rangle}} = -\frac{\langle \overline{w}\,\overline{\varphi} \rangle}{\overline{\langle w''\varphi'' \rangle}} \tag{4b}$$

where $\langle I_\varphi \rangle$ represents the mean or expected value of flux imbalance with the EC measurement, $\left\langle \overline{w'\varphi'} \right\rangle$ is the scalar flux measured by the EC method and averaged spatially in the x–y direction, and $\overline{\langle w''\varphi'' \rangle}$ is the total flux. According to Eq. 4b, a flux imbalance exists if there is a spatial covariance between the temporally averaged mean vertical velocity and the scalar concentration ($\langle \overline{w}\,\overline{\varphi} \rangle$). The reader is also reminded of the sign convention we use throughout the paper: a negative $\langle I_\varphi \rangle$ indicates underestimation of flux by the EC method or the Reynolds-averaging procedure, and vice versa. Unless stated otherwise, the subfilter-scale (SFS) contribution to the flux is added to both $\left\langle \overline{w'\varphi'} \right\rangle$ and $\overline{\langle w''\varphi'' \rangle}$ before computing the flux imbalance and their vertical profiles.

3 The LES Model

The NCAR's LES model, originally described by Moeng (1984) and Sullivan et al. (1996) and subsequently modified by Patton et al. (2005), is used in this study. The LES model solves the Navier-Stokes equations for the resolvable scale velocity components (u, v, w), a thermodynamic equation for resolvable potential temperature field (θ), and a Poisson equation for pressure in an incompressible flow field. The SFS fluxes contained in the momentum and scalar equations are determined from the resolved-scale variables and the SFS kinetic energy. To determine the SFS turbulence kinetic energy, we solve the prognostic model described by Deardorff (1980). The resolvable variables are solved by using pseudo-spectral and finite-difference methods to calculate horizontal and vertical derivatives, respectively. Periodic boundary conditions are imposed in the horizontal directions and the radiative boundary conditions of Klemp and Durran (1983) are set at the upper boundaries. At the surface, Monin-Obukhov similarity (Businger et al. 1971) is assumed.

In this study, three sets of LES model simulations, labeled as A, B and C in Table 1, were conducted at a horizontal grid spacing of 50 m × 50 m and a vertical resolution of 20 m over a domain with size of 5 km × 5 km × 1.92 km in the x, y, and z directions, respectively. Simulations were run with geostrophic winds of 0, 2, 4, and 6 m s^{-1} and with a surface heat flux of either 0.1 or 0.02 K m s^{-1}. The two surface heat flux values, representing moderate and weak surface thermal forcing, result in a convective velocity (w_*) that differs by roughly a factor of two. The convective velocity (w_*) is defined as $\left(\frac{g\overline{w\theta_0}z_i}{T}\right)^{\frac{1}{3}}$, where T is a reference potential temperature, $\overline{w\theta_0}$ is the surface heat flux, g is gravity acceleration, and z_i is the mixing-layer height. The change of w_* is a useful feature of this study since w_* is a velocity scale that aids the development of nondimensional functions of the flux imbalance. The fourth simulation, labeled as D in Table 1, was carried out at a finer grid resolution of 25 m × 25 m × 10 m. The last three cases, labeled as E, F, and G in Table 1, were designed to examine the impact of

Table 1 Summary of LES model configurations

Case	Domain size (km)	Grid resolution (m)	u_g (m s^{-1})	Surface heat flux (K m s^{-1})	Surface χ_b flux (mg kg^{-1} m s^{-1})	Initial z_i (m)	z_i/L
A.0	$5 \times 5 \times 1.92$	$50 \times 50 \times 20$	0	0.02	0.101	840	−267.9
A.2	$5 \times 5 \times 1.92$	$50 \times 50 \times 20$	2	0.02	0.101	840	−65.4
A.4	$5 \times 5 \times 1.92$	$50 \times 50 \times 20$	4	0.02	0.101	840	−16.2
A.6	$5 \times 5 \times 1.92$	$50 \times 50 \times 20$	6	0.02	0.101	840	−6.5
B.0	$5 \times 5 \times 1.92$	$50 \times 50 \times 20$	0	0.1	0.505	960	−348.8
B.2	$5 \times 5 \times 1.92$	$50 \times 50 \times 20$	2	0.1	0.505	960	−201.7
B.4	$5 \times 5 \times 1.92$	$50 \times 50 \times 20$	4	0.1	0.505	960	−62.2
B.6	$5 \times 5 \times 1.92$	$50 \times 50 \times 20$	6	0.1	0.505	960	−27.6
C.0	$5 \times 5 \times 1.92$	$50 \times 50 \times 20$	0	0.1	0.505	1240	−276.4
C.2	$5 \times 5 \times 1.92$	$50 \times 50 \times 20$	2	0.1	0.505	1240	−229.4
D	$5 \times 5 \times 1.92$	$25 \times 25 \times 10$	0	0.02	0.101	840	−249.9
E	$5 \times 5 \times 1.92$	$50 \times 50 \times 20$	0	0.2	1.010	840	−243.0
F	$5 \times 5 \times 1.92$	$50 \times 50 \times 20$	0	0.3	1.515	840	−289.0
G	$5 \times 5 \times 1.92$	$50 \times 50 \times 20$	0	0.4	2.020	840	−329.7

surface heat flux on the imbalance flux under free convection. The configurations of cases E–G are the same as those of case A except for the surface heat flux. In all simulations, a roughness length (z_0) of 0.1 m was used, and the surface was horizontally homogeneous.

In order to study the influence of entrainment and bottom–up diffusion on the profiles of the flux and flux imbalance, two scalars, a top–down tracer (χ_t) and a bottom–up tracer (χ_b), were implemented in the LES model to represent top–down and bottom–up diffusion. The top–down diffusion was characterized by a non-zero flux at the mixed-layer top and a zero flux at the surface. Specifically, a gradient was specified for the initial χ_t mixing ratio in the interfacial layer, allowing entrainment to generate a negative or downward χ_t flux at the top of the mixed layer. The bottom–up diffusion was represented by a non-zero flux at the surface (Table 1) and specified by a constant initial χ_b mixing ratio profile throughout the domain.

The LES simulations were initiated with profiles of θ, χ_t, and χ_b that were specified uniformly in the horizontal directions of the model domain. The initial θ profile was set to a constant $\theta = 300.0$ K within the mixed layer (defined as the air layer below $z_i - 40$ m, where z_i is mixing-layer height), a vertical gradient of 0.0375 K m^{-1} in the interfacial layer (defined as a layer between $z_i - 40$ m and $z_i + 40$ m), and a vertical gradient of 0.003 K m^{-1} above the interfacial layer (above $z_i + 40$ m). The temperature gradient across the interfacial layer generated an entrainment flux that was typically 20% in magnitude of the heat flux at the surface. The heat diffusion in the PBL is therefore a combination of both top–down and bottom–up processes (Jonker et al. 1999). In comparison, the inversion jump in K04 and S07 was 0.0074 K m^{-1}, which is much weaker than ours. Thus their top–down flux generated by the entrainment process should be negligibly small.

The initial mixing ratio profile of χ_b was set to a constant value of 531.0 mg kg^{-1} throughout the entire domain. The initial profile of χ_t consisted of a value of 531.0 mg kg^{-1} within the mixed layer, a strong gradient of 0.375 mg kg^{-1} m^{-1} across the interfacial layer and a constant value of 561.0 mg kg^{-1} above the interfacial layer. The surface χ_b flux for each run is given in Table 1.

The post-processing analyses of the LES data are performed after the turbulent kinetic energy has reached a quasi-steady state (Patton et al. 2005), usually after about 120 min of

integration time. The timesteps during each simulation are dynamically determined based on the Courant-Friedrichs-Lewy (CFL) number. All temporal averaging is performed over the 60-min interval after steady state has been established. The 60-min averaging is typical of field measurements using EC, and the number of timesteps that one-hour averaging requires increases slightly as the surface heat flux increases. The reader should be aware that the imbalance statistics may change if a different averaging period is used (K04). K04 found that a three-hour averaging gives slightly smaller biases and larger variances of the imbalance as compared to the one-hour averaging. We also found similar results.

The Reynolds statistics are computed online for all grid points with a routine embedded in the LES model. As an illustration, the Reynolds covariance between w and scalar φ at a given grid point is given by

$$\overline{w'\varphi'} = \frac{1}{N}\sum_{i=1}^{N}(w_i - \overline{w})(\varphi_i - \overline{\varphi}) = \frac{1}{N}\sum_{i=1}^{N} w_i\varphi_i - \frac{1}{N^2}\sum_{i=1}^{N} w_i \sum_{i=1}^{N}\varphi_i \tag{5}$$

where N is the total number of timesteps during the averaging period, and w_i and φ_i are the model-predicted instantaneous fields at time $t = t_i$. The online routine is activated after the steady state has been reached. It updates all the summation terms, such as $\sum_{i=1}^{N} w_i\varphi_i$, $\sum_{i=1}^{N} w_i$, and $\sum_{i=1}^{N}\varphi_i$, which are needed for the computation of Reynolds statistics, at each timestep. At every 100 timesteps, these summation terms are saved in a temporary file. Hourly statistics are computed from the summation terms after the simulation is completed. Strictly, Eq. 5 requires that the sampling timestep be constant. In the LES simulations, the timestep typically varies from 2.8 to 3.2 s. Computations using eddy covariance time series obtained in a real field experiment in midday, convective conditions indicate that the variable timestep has a negligible effect on the Reynolds flux.

4 Results and Discussion

4.1 Imbalance of Heat, Top–down, and Bottom–up Fluxes

Figure 1 shows the profiles of the spatial (denoted as $\overline{\langle w''\varphi''\rangle}$ for convenience of discussion) and Reynolds $\left(\left\langle\overline{w'\varphi'}\right\rangle\right)$ averaged fluxes of heat, the bottom–up, and the top–down tracer as a function of normalized height (z/z_i) for case B with $u_g = 0\,\mathrm{m\,s^{-1}}$. The fluxes of heat and the bottom–up tracer are normalized with their respective surface value while that of the top–down tracer is normalized with its entrainment flux. The mixed-layer height z_i is defined as the height where the potential temperature gradient reaches its maximum value. The growth rate of z_i due to entrainment is about $7\,\mathrm{mm\,s^{-1}}$ during the simulation period. The profiles of the spatially-averaged fluxes follow a linear dependence with height, indicating that the flow field has reached steady state. The spatially-averaged heat flux $\overline{\langle w''\theta''\rangle}$ decreases linearly from the surface flux to 20% of its surface value at the mixed-layer top. The bottom–up tracer does not show zero flux at the mixed-layer top while the top–down tracers show a negligible flux at the surface. With a surface source, the bottom–up tracer has an influence from entrainment due to an increase in the scalar mean concentration within the PBL vs. zero above. For example, the flux of the bottom–up tracer generated by the entrainment process at the mixed-layer top is about 4.5% of the flux at the surface (Fig. 1b).

In comparison to their spatial counterparts, the profiles of the Reynolds-averaged fluxes are distinctly curved. The degree of the flux underestimation depends on the location of the

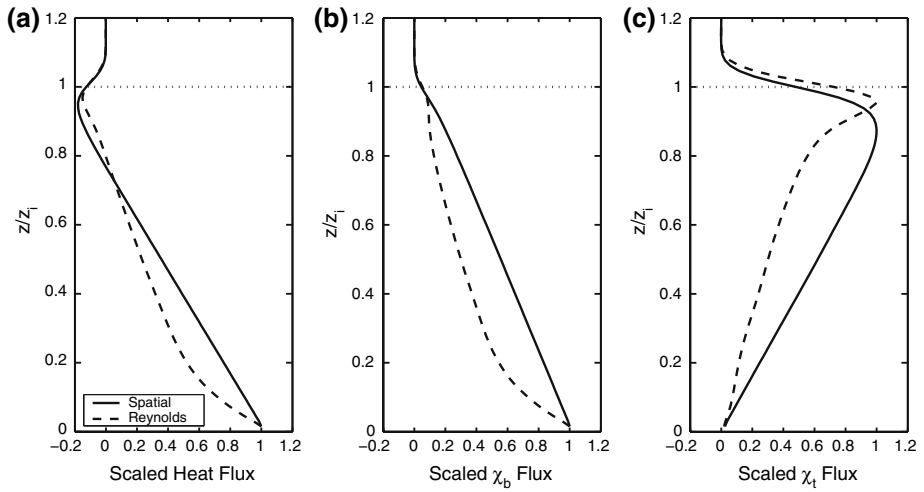

Fig. 1 Profiles of spatial and Reynolds-averaged fluxes (normalized with the surface or entrainment flux) of (**a**) heat, (**b**) the bottom–up tracer (χ_b), and (**c**) the top–down tracer (χ_t) over the whole domain for the case B at $u_g = 0\,\mathrm{m\,s^{-1}}$ (solid line: spatial averaging flux, dash line: temporal averaging flux, dotted line: the top of the PBL). The averaging time period covers $t_p = 1.8$–$2.8\,\mathrm{h}$. Note that the turbulent statistics reaches the steady-state at the simulated time 1.8 h

source and the measurement height in the boundary layer. Both the fluxes of heat and the bottom–up tracer are underestimated most in the lower part of the PBL, at about $z = 0.2z_i$, whereas the flux of the top–down tracer is underestimated most in the upper part of the PBL, at about $z = 0.8z_i$. The degree of flux underestimation for the top–down tracer is striking. As an example, for the case B with $u_g = 0\,\mathrm{m\,s^{-1}}$, the Reynolds flux $\left\langle \overline{w'\chi_t'} \right\rangle$ is $-0.12\,\mathrm{mg\,kg^{-1}\,m\,s^{-1}}$ at $z = 0.8z_i$, which is only 38% of the spatial flux, or a flux imbalance of -62%.

The flux of any scalar, φ, in the PBL can be treated as a linear superposition of top–down and bottom–up diffusion (Wyngaard and Brost 1984; Jonker et al. 1999). Using the simulations of tracers χ_t and χ_b, we can construct the flux of any other scalar with different entrainment/bottom–up flux ratios. Under the quasi-steady state condition, the linear superposition principle yields the following relationships

$$\left\langle \overline{w'\varphi'} \right\rangle = \left\langle \overline{w'\chi_t'} \right\rangle + \left\langle \overline{w'\chi_b'} \right\rangle, \tag{6a}$$

$$\overline{\langle w''\varphi'' \rangle} = \overline{\left\langle w''\chi_t'' \right\rangle} + \overline{\left\langle w''\chi_b'' \right\rangle}, \tag{6b}$$

where $\varphi = \chi_t + \chi_b$. Substitution of Eqs. 6a and b into Eq. 4b yields an expression for the flux imbalance of scalar φ

$$\left\langle I_\varphi \right\rangle = \frac{\overline{\left\langle w''\chi_t'' \right\rangle}}{\overline{\langle w''\varphi'' \rangle}} \langle I_t \rangle + \frac{\overline{\left\langle w''\chi_b'' \right\rangle}}{\overline{\langle w''\varphi'' \rangle}} \langle I_b \rangle \tag{7}$$

where $\langle I_t \rangle$ and $\langle I_b \rangle$ are flux imbalances of the diffusion from the top and bottom sources, respectively, and are determined by the LES simulation of the two tracers χ_t and χ_b, respectively. Since the spatial fluxes $\overline{\left\langle w''\chi_t'' \right\rangle}$ and $\overline{\left\langle w''\chi_b'' \right\rangle}$ follow a linear dependence with height, Eq. 7 becomes

$$\langle I_\varphi \rangle = \frac{\overline{\langle F_{t,0} \rangle}}{\langle w''\varphi'' \rangle} \langle I_t \rangle \frac{z}{z_i} + \frac{\overline{\langle F_{b,0} \rangle}}{\langle w''\varphi'' \rangle} \langle I_b \rangle \left(1 - \frac{z}{z_i}\right) \tag{8}$$

where $\overline{\langle F_{t,0} \rangle}$ is the (top–down) flux of tracer χ_t at z_i and $\overline{\langle F_{b,0} \rangle}$ is the (bottom–up) flux of χ_b at the surface. According to Eq. 8, the flux imbalance of φ is influenced by both the entrainment at the PBL top through the top–down diffusion and the surface exchange through the bottom–up diffusion. The strength of the top–down and bottom–up influences depends on the vertical distance from these sources and the strength of the surface and entrainment fluxes. The imbalance profile for any scalar can therefore be constructed from the profiles of $\langle I_t \rangle$ and $\langle I_b \rangle$ so long as the top and bottom flux boundary conditions, $\overline{\langle F_{t,0} \rangle}$ and $\overline{\langle F_{b,0} \rangle}$, are known. Eq. 8, although appearing complex, is actually simple to use because the spatial fluxes (e.g. $\overline{\langle w''\varphi'' \rangle}$) are all linear with height within the PBL: $\overline{\langle w''\varphi'' \rangle}$ will change from $\overline{\langle F_{b,0} \rangle}$ at $z = 0$ linearly to $\overline{\langle F_{t,0} \rangle}$ at $z = z_i$, and so on. For example, for heat diffusion in case B with $u_g = 0\,\mathrm{m\,s^{-1}}$, $\overline{\langle F_{t,0} \rangle} \approx -0.02\,\mathrm{K\,m\,s^{-1}}$ and $\overline{\langle F_{b,0} \rangle} \approx 0.1\,\mathrm{K\,m\,s^{-1}}$, and the reconstructed flux imbalance is indistinguishable from the calculation using the LES-simulated Reynolds and spatial heat flux (data not shown).

Let r_f be the ratio of the entrainment flux to surface flux. For convenience, we define a ratio angle as $\psi = \arctan\left(\frac{1}{r_f}\right)$, and accordingly, Eq. 8 becomes

$$\langle I_\varphi \rangle = \frac{\overline{\langle F_{b,0} \rangle}}{\langle w''\varphi'' \rangle} \left[r_f \langle I_t \rangle \frac{z}{z_i} + \langle I_b \rangle \left(1 - \frac{z}{z_i}\right) \right]. \tag{8a}$$

The dependence of $\langle I_\varphi \rangle$ on r_f at different $\frac{z}{z_i}$ for case B under the free convection condition is plotted in Fig. 2, up to $z = 0.72 z_i$ since the spatially-averaged flux $\overline{\langle w''\varphi'' \rangle}$ changes from positive to negative at that height.

As demonstrated in Fig. 2, the vertical profiles of flux imbalance display a complex non-linear relationship to the ratio of the entrainment flux to the surface flux. When the flux ratio is positive ($\psi < 90°$, e.g. CO_2 in the daytime) or negative but $\psi < 115°$, the magnitude of the flux underestimation increases monotonically with height. It is very clear that a higher flux ratio exerts a more important influence on the flux imbalance. When $\psi > 115°$ (i.e., the flux ratio is negative, as with heat flux), the flux imbalance increases with height in the lower part of the PBL, and then deceases as with increasing height above the height of zero flux. Furthermore, when the flux ratio decreases to a larger negative value (i.e., $\psi > 145°$), a positive flux imbalance appears in the middle to upper parts of the PBL. However, if ψ is in the region of 115°, the flux imbalance exhibits a uniform distribution in the middle part of the PBL.

4.2 Imbalance Probability Distribution

The probability function is a useful statistical parameter to characterize the behaviour of flux imbalance in the convective PBL. Figure 3 shows that the probability distribution of flux imbalance for heat, the top–down and the bottom–up tracer at several heights for case B with $u_g = 0\,\mathrm{m\,s^{-1}}$. The imbalance probability for heat shifts to more negative values and shows a much wider spread as the measurement height increases. For example, the peak probability occurs at an imbalance value of -10% at the height of $z = 20\,\mathrm{m}$ and -44% at the height of $z = 100\,\mathrm{m}$. Our results are in excellent agreement with those of both K04 and S07. The imbalance probability of the bottom–up tracer displays a similar changing trend with height

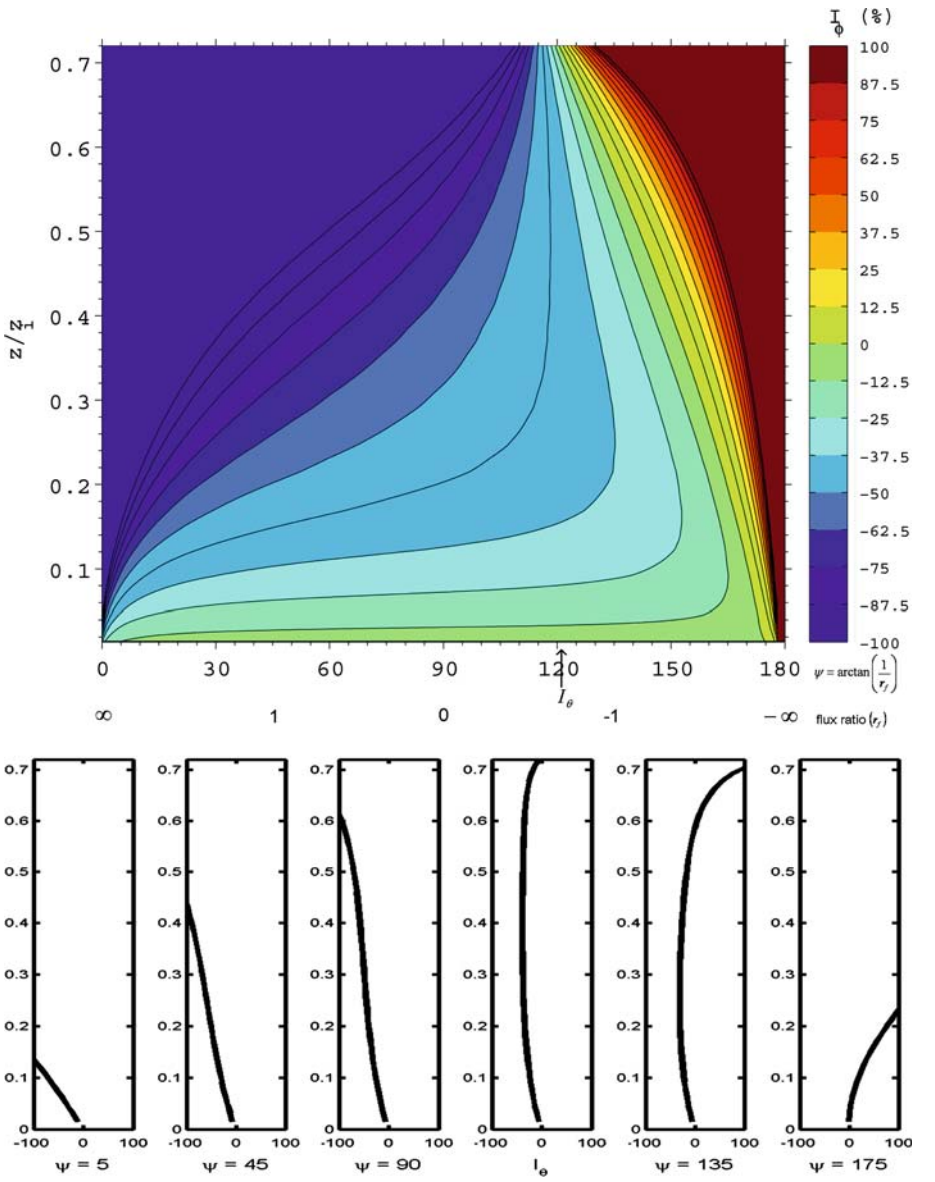

Fig. 2 The flux imbalance of any scalar plotted as a function of the normalized height (z/z_i) and the ratio angle ($\psi = \arctan\left(\frac{1}{r_f}\right)$) of entrainment to surface flux. The vertical flux imbalance profiles of heat as well as any other scalar at several flux ratio angles are displayed at the bottom of the figure. The arrow points to the flux ratio angle for potential temperature

as heat, at least in the lower PBL, because heat flux there is dominated by bottom–up diffusion (Fig. 3b).

However, for the top–down tracer, the imbalance probability is quantitatively different from those for heat and the bottom–up tracer. It is skewed to considerably more negative values and occurs in a much broader range near the top of the PBL, where the impact of

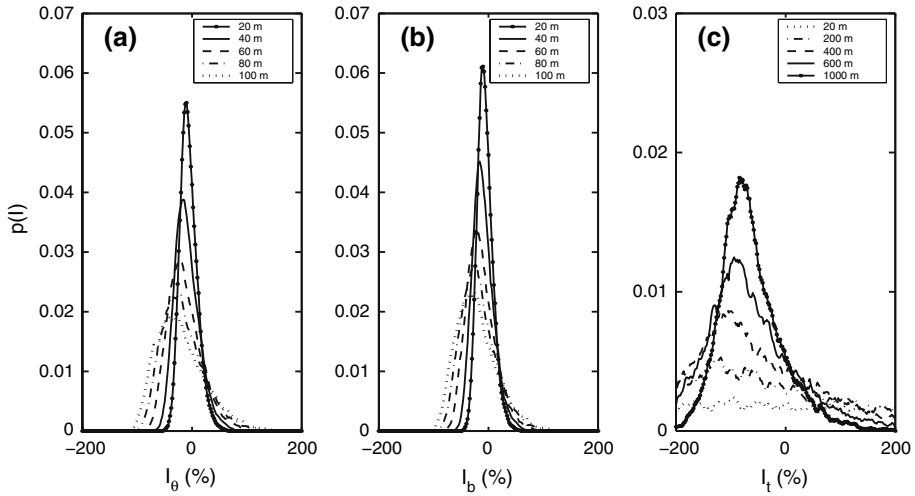

Fig. 3 Probability functions of flux imbalance of (**a**) heat (I_θ), (**b**) the bottom–up tracer (I_b), and (**c**) the top–down tracer (I_t) at different heights for the same case as shown in Fig. 1

entrainment is larger than the values found in the lower PBL. The peak probability is found at an imbalance of -84% at the height of $z = 1{,}000\,\mathrm{m}$ and -98% at the height $z = 600\,\mathrm{m}$ for case B with $u_g = 0\,\mathrm{m\,s^{-1}}$. Below the height of $z = 200\,\mathrm{m}$, the peak probability is hard to define as the imbalance function behaves as white noise.

Figure 4 shows the profiles of the flux imbalance standard deviation (σ_I) for the same LES simulation as in Figs. 1 and 3. For the bottom–up tracer, σ_I is lowest near the ground, increases slowly with height to approximately 100% at $z/z_i = 0.73$, and then increases dramatically near the PBL top. For the top–down tracer, σ_I is extremely large ($> 400\%$) near the ground and reaches the lowest value of 50% at $z/z_i = 0.8$. For heat, σ_I is generally larger than that for the bottom–up tracer, and reaches extremely large values near$z/z_i = 0.7$ where the flux profile crosses the zero value (Fig. 1a). Thus, source location is a critical factor that controls the spatial variability of flux imbalance. In situations where the top–down influence is profound, the near-surface fluxes measured by the EC method will be inherently noisy.

Compared with free convection, the imbalance probability of heat and the tracer χ_b exhibits a distinct feature when u_g is greater than $0\,\mathrm{m\,s^{-1}}$ (data not shown). As u_g increases, the probability distribution becomes steeper, including a higher peak and a narrower width. For example, at $z = 20\,\mathrm{m}$, the imbalance probability of heat flux has a peak of 5.8% at the imbalance of -10% for $u_g = 0\,\mathrm{m\,s^{-1}}$, 7.8% at -2% for $u_g = 2\,\mathrm{m\,s^{-1}}$, 12.8% at -2% for $u_g = 4\,\mathrm{m\,s^{-1}}$, and 15.1% at -2% for $u_g = 6\,\mathrm{m\,s^{-1}}$. Thus, heat flux tends to be underestimated by Reynolds averaging by about 2% when u_g is greater than $4\,\mathrm{m\,s^{-1}}$.

Consistent with the probability distribution, the magnitude of the standard deviation becomes smaller as u_g increases, indicating that the spatial variability of flux imbalance decrease with increasing u_g (figure not shown).

4.3 Universal Functions of Flux Imbalance

The above discussion has relied mostly on one LES simulation under free convection to examine the dependence of flux imbalance on the measurement height and on the roles of the top–down and bottom–up diffusion. It is also known, through modelling studies (K04

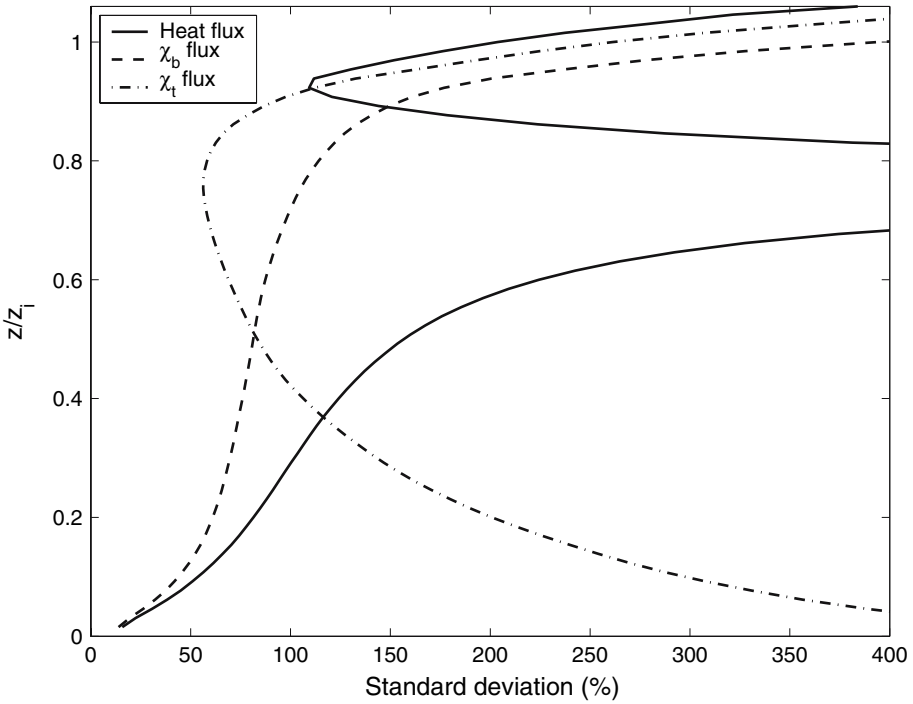

Fig. 4 Standard deviation of flux imbalance for heat (solid line), the bottom–up tracer (χ_b, dash line), and the top–down tracer (χ_t, dash–dot line) for the same case as shown in Figs. 1 and 3

and S07) and field observations (Lee 1998; Mahrt 1988), that as wind speed increases, flux imbalance will decrease. In addition, S07 found that the surface heat flux itself will influence the heat flux imbalance. To quantify the combined effects of the above-mentioned parameters, we propose that flux imbalance can be described by

$$\langle I \rangle = -f\left(z, z_i, u_*, w_*\right). \tag{9}$$

The independent variables in Eq. 9 can be used to form two non-dimensional variables, z/z_i and u_*/w_*. Further, it is assumed that f in Eq. 9 is the product of two different functions, formulated as

$$<I> = -f_1\left(\frac{u_*}{w_*}\right) f_2\left(\frac{z}{z_i}\right), \tag{10}$$

The non-dimensional functions have a desirable feature in that they reduce the number of controlling variables to fewer non-dimensional parameters.

4.3.1 The Dependence on Friction Velocity and Surface Heating

In Fig. 5, the flux imbalance of the bottom–up tracer, averaged over the layer $z/z_i = 0.3$ to 0.5 is plotted as a function of u_*/w_*. Here friction velocity is defined as $u_* = \left(\left(-\overline{\langle u''w''\rangle}\right)^2 + \left(-\overline{\langle v''w''\rangle}\right)^2\right)^{0.25}$, where $\overline{\langle u''w''\rangle}$ and $\overline{\langle v''w''\rangle}$ are the longitudinal and

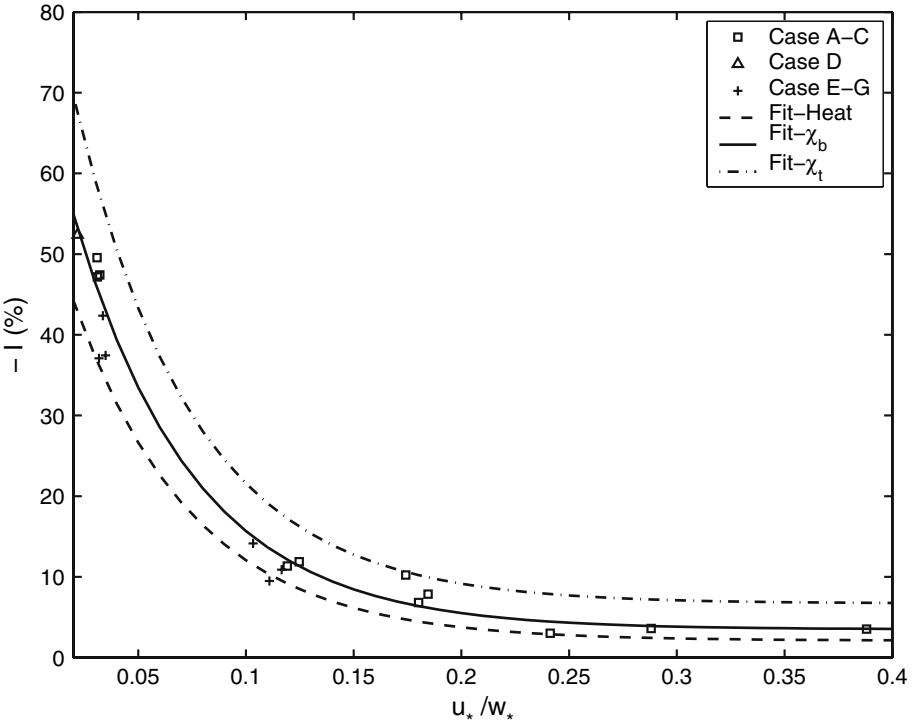

Fig. 5 Simulated flux imbalance averaged over 0.3 to $0.5 z/z_i$ (squares: cases A–C, triangle: case D, and plus: cases E–G) and the non-dimensional curves of flux imbalance (solid line: the bottom–up tracer (Fit-χ_b), dash line: heat (Fit-Heat), and dotted lines: the top–down tracer (Fit-χ_t))

lateral components, respectively, of the domain-averaged momentum flux at the first grid height. For clarity, only data for the flux imbalance of the bottom–up tracer are shown in the Figure. Each data point in the plot represents a LES simulation with one combination of u_* and w_* given in Table 1. The imbalance decreases rapidly with increasing u_*/w_*, consistent with K04 and S07, although in K04 and S07 the imbalance is shown as a function of the dimensional velocity u_g. The flux imbalance for heat and tracer χ_t follows a similar pattern. The data in Fig. 5 suggest the following function for f_1 in Eq. 10

$$f_1 = \exp\left(d_1 + d_2 \frac{u_*}{w_*}\right) + d_3. \tag{11a}$$

The three coefficients in Eq. 11a are found by regression against the LES data (Table 2). At the upper limit of the u_*/w_* value of our LES simulations, the flux imbalance approaches a non-zero value of d_3. In other words, even in relatively strong winds or weak surface heat flux, the EC measurement will underestimate by 2 to 7% the true flux in the air layer $z/z_i = 0.3 - 0.5$.

Equation 11a represents well the flux imbalance under both free ($u_g = 0\,\mathrm{m\,s^{-1}}$) and forced ($u_g > 0\,\mathrm{m\,s^{-1}}$) convection conditions. The non-dimensional velocity u_*/w_* provides a better description of the imbalance than both dimensional velocity u_g and non-dimensional velocity u_g/w_*. As shown in Table 3, a clear decreasing trend of the flux imbalance is observed when the surface heat flux increases from 0.05 to $0.4\,\mathrm{K\,m\,s^{-1}}$. A similar trend was also reported by

Table 2 The coefficients of non-dimensional functions describing heat, top–down (χ_t), and bottom–up (χ_b) flux imbalance

Coefficient	Heat flux imbalance	χ_b flux imbalance	χ_t flux imbalance
d_1	4.2	4.3	4.7
d_4	−16.0	−16.0	−16.0
d_3	2.1	3.5	6.7
d_4	−8.0	−6.2	−4.5
d_5	−0.38	−0.45	−0.4

Table 3 The averaged mixed-layer height (z_i), convective velocity scale (w_*), surface friction velocity (u_*), and the flux imbalance of heat, χ_b, and χ_t under free convection condition

Case	Averaged z_i (m)	w_* (m s^{-1})	u_* (m s^{-1})	$<I>_\theta$ (%)	$<I>_b$ (%)	$<I>_t$ (%)
A	860	0.82	0.025	−41.0	−49.6	−74.5
B	1050	1.51	0.047	−37.0	−47.2	−72.9
C	1350	1.64	0.053	−39.5	−47.4	−71.7
D	860	0.82	0.018	−47.7	−54.0	−89.0
E	950	1.84	0.062	−32.6	−42.4	−67.8
F	1010	2.14	0.068	−30.0	−37.1	−53.3
G	1110	2.44	0.085	−29.0	−37.5	−53.4

The flux imbalance is averaged over the layer of $z/z_i = 0.3$–0.5

S07. The flux imbalance shows a nonlinear dependence on the surface heat flux and a linear dependence on friction velocity and the convective velocity scale. The universal function illustrated in Eq. 11a represents well the flux imbalance under the two convection regimes through the dimensionless velocity u_*/w_*.

4.3.2 The Influence of Measurement Height

The imbalance normalized by Eq. 11a is plotted as a function of z/z_i in Fig. 6 for the first four LES runs (i.e., cases A–D) with $u_g = 0\,\mathrm{m\,s^{-1}}$ (free convection condition, Table 1). The normalized heat flux imbalance increases with height to the maximum value at $z = 0.35z_i$, and decreases slowly with further increase in height. The bottom–up tracer shows a slightly different imbalance profile, which increases with increasing height and approaches a constant value beyond the height of $0.5z_i$. The imbalance of the top–down tracer shows a uniform distribution in the middle of PBL with a slight change near the surface. The results from K04 and S07 obtained for free convection conditions agree well with ours. The good agreement is a strong piece of evidence showing that their results are robust and are not an artifact of model numerical schemes. The second function in Eq. 10 can be described by

$$f_2\left(\frac{z}{z_i}\right) = \left(1.1 + d_4\left(\frac{z}{z_i} + d_5\right)^2\right)^{\frac{1}{2}} \tag{11b}$$

($z/z_i \le 0.5$), where the empirical parameters d_4 and d_5 are given in Table 2 for heat, the top–down and the bottom–up tracers. The non-dimensional functions, which are restricted to the air layer below $z = 0.5z_i$ to avoid the zero-crossing of the heat flux, match quite well with the LES model simulations of the single-source diffusion problem (top–down and bottom–up tracers, Fig. 6). In comparison, more scatter is evident in the heat imbalance profile.

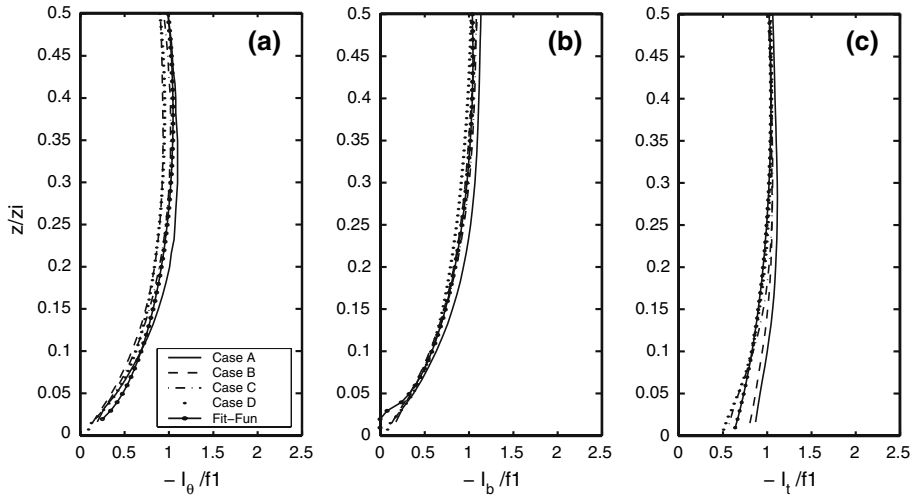

Fig. 6 Normalized flux imbalance of (**a**) heat, (**b**) the bottom–up tracer, and (**c**) the top–down tracer as well as their respective non-dimensional functions plotted against z/z_i at free convection condition. (solid line: case A, dash line: case B, dash–dot line: case C, point: case D, solid line with triangle: non-dimensional function)

The above non-dimensional functions (Eqs. 9–11) offer useful diagnostic information on when the EC measurement likely underestimates the flux. The studies of K04 and S07 have established the dependence of the flux imbalance on u_g and the measurement height z. Our work extends their results by casting the relationship in a non-dimensional form. The flux imbalance decreases exponentially with the increase of the normalized wind u_*/w_*, and increases with the normalized height z/z_i following an elliptic function in the lower boundary layer. Two features deduced from Eqs. 9–11 deserve attention. First, under free convection, the EC measurement in the lower PBL will severely underestimate the true flux when the mixed layer is shallow. Second, under non-zero geostrophic wind, the sensitivity to z_i is complex as z_i affects both u_*/w_* and z/z_i.

4.4 Sensitivity to Domain Size and Grid-spacing

In order to examine the sensitivity of the results to the model domain size, we did two more simulations over a larger horizontal domain size of $9.6 \times 9.6\,\mathrm{km}^2$, forced by the same configurations as the cases B.0 and B.6 in Table 1. The difference in the heat flux imbalance averaged over the layer $z/z_i = 0.3-0.5$ is 0.9% (−38.8% for the B.0 domain versus −37.9% for the enlarged domain) at $u_g = 0$ and 0.5 % (−3.0% vs. −2.5%) at $u_g = 6\,\mathrm{m\,s}^{-1}$. The small difference is not surprising in the $u_g = 0\,\mathrm{m\,s}^{-1}$ case since the characteristic turbulent structures should be well represented by the default domain for this forcing. In free convection, the turbulent structures should all be hexagonal cell-like with length scales that are tied to the depth of the PBL. Since the default domain is about five times larger horizontally than the characteristic length scale, the LES statistics should be reasonably captured by the default domain. In the cases that are more shear-dominated, large roll-like structures should form that are much longer in one direction than the PBL is deep. However, our sensitivity test shows that the difference is within the margin of computational errors for $u_g > 0\,\mathrm{m\,s}^{-1}$, indicating that the original domain size is appropriate.

In order to illustrate the influence of grid-spacing on flux imbalance, we conducted a fine resolution LES run (case D, Table 1). The results are presented in Table 3 and Fig. 6. Compared with case A, the flux imbalance averaged over the layer $z/z_i = 0.3$–0.5 for case D the flux imbalance is higher by 6.9%, 5.6%, and 14.0% for heat, tracer χ_b, and χ_t, respectively. There are two possible reasons for this response. First, more small-scale components of the velocity and scalar fields are resolved with a finer grid-spacing. Second, the spatial fluctuations of the vertical velocity and the scalar concentrations seem to have intensified slightly as the grid-spacing becomes smaller, which leads to an increase in the spatial covariance of the time-averaged quantities. In general, the sensitivity to grid-scaling does not modify the shape of the flux imbalance profiles.

4.5 Spatial Coherence

We now turn our attention to the spatial coherence of flux imbalance and the velocity as well as scalar fields in the x–y directions. It is worth recalling from Eq. 4b that the non-zero spatial covariance between the Reynolds mean vertical velocity ($\overline{w}$), and the mean scalar concentration ($\overline{\varphi}$), $\langle \overline{w}\,\overline{\varphi} \rangle$, is ultimately responsible for the flux imbalance. Figure 7 shows the profiles of the spatial covariance of $\overline{w}$ and $\overline{\theta}$, $\overline{w}$ and $\overline{\chi_b}$, as well as $\overline{w}$ and $\overline{\chi_t}$ ($\langle \overline{w}\,\overline{\varphi} \rangle$, solid line), along with the profiles of their counterparts of $\overline{\langle w''\varphi'' \rangle}$ (dashed line, spatial averaging flux) and $\left\langle \overline{w'\varphi'} \right\rangle$ (dash–dotted line, Reynolds flux) for two geostrophic winds, 0 and $4\,\mathrm{m\,s^{-1}}$. The spatial covariance, $\langle \overline{w}\,\overline{\varphi} \rangle$ accounts exactly for the difference between the spatial averaging flux and the Reynolds flux, or flux imbalance, as required by the definitions of these two averaging operations (Eq. 3a and b). Under free convection conditions, both $\left\langle \overline{w}\,\overline{\theta} \right\rangle$ and $\left\langle \overline{w}\,\overline{\chi_b} \right\rangle$ peak at $z/z_i = 0.2$, suggesting that TOS is most efficient in transporting heat and the bottom–up tracer at this height. Below this height especially near the surface, transport due to the SFS turbulent motion becomes important. In contrast, the peak of the spatial covariance of the mean Reynolds vertical velocity and the mean top–down tracer concentration, $\langle \overline{w}\,\overline{\chi_t} \rangle$ is located at the upper PBL. The $\langle \overline{w}\,\overline{\varphi} \rangle$ profiles appear smoother at $u_g = 4\,\mathrm{m\,s^{-1}}$ than those under free convection conditions.

Physically, the spatial covariance $\langle \overline{w}\,\overline{\varphi} \rangle$ arises from the existence of TOS. The TOS structures include two parts, a network of narrow bands of isotherms and a set of wider polygon-like regions (Figs. 8a and b). The former demarks warmer updraft regions (positive $\overline{w}$) while the latter corresponds to cooler downdraft regions (negative $\overline{w}$). Such TOS structures are well documented in the LES literature (K04 and S07). As u_g increases, the TOS structures become more longitudinal and even evolve into roll structures when the wind shear dominates the PBL. The contour plot of $\overline{\chi_b}$ brings out patterns that bear remarkable resemblance to those of $\overline{w}$ and $\overline{\theta}$ (Fig. 8c). Such resemblance is lost with the top–down tracer, $\overline{\chi_t}$ (Fig. 8d).

Figure 9 shows the spatial distribution of flux imbalance of heat (Fig. 9a), the bottom–up tracer (Fig. 9b) and the top–down tracer (Fig. 9c), for the height of 100 m from the same LES simulation as shown in Fig. 8. In general, regions of positive imbalance of heat and the bottom–up tracer correspond to regions of updrafts (Fig. 8a), and vice versa. Since the total area of downdrafts is much bigger than that of updrafts (Fig. 8a), it is no surprise that the area-averaged flux imbalance $\langle I \rangle$ is negative and that the I probability functions are skewed toward negative values (Fig. 3). At this height, there is little correspondence between the flux imbalance of the top–down tracer (Fig. 9c) and the vertical velocity field (Fig. 8a).

K04 showed that the heat flux imbalance I_θ at any grid point is not well-correlated with the Reynolds-averaged vertical motion ($\overline{w}$). In the case shown in Figs. 8 and 9, the linear

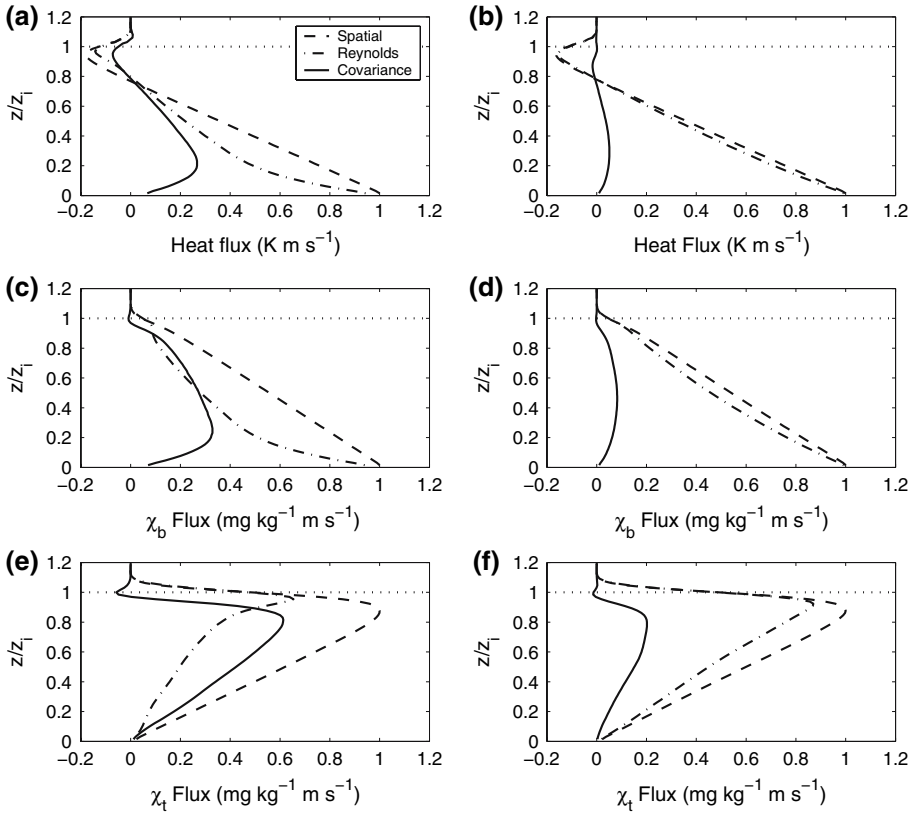

Fig. 7 Spatial and Reynolds-averaged fluxes for (**a**) and (**b**) heat, (**c**) and (**d**) the bottom–up tracer (χ_b), (**e**) and (**f**) the top–down tracer (χ_t) ((**a**), (**c**), and (**e**) for $u_g = 0\,\mathrm{m\,s^{-1}}$; (**b**), (**d**), and (**f**) for $u_g = 4\,\mathrm{m\,s^{-1}}$), spatial covariance, $\langle \overline{w}\,\overline{\theta} \rangle$, $\langle \overline{w}\,\overline{\chi_b} \rangle$, $\langle \overline{w}\,\overline{\chi_t} \rangle$ are also included (solid line: spatial averaged flux, (spatial, $\overline{\langle w'\varphi' \rangle}$), dash line: Reynolds averaging (Reynolds, $\langle \overline{w'\varphi'} \rangle$), dash-dot line: spatial covariance of $\overline{w}$ and mean scalar (Covariance, $\langle \overline{w}\,\overline{\varphi} \rangle$), dotted line: the top of the PBL). The averaging time period covers $t_p = 1.8$–$2.8\,\mathrm{h}$, height $z = 100\,\mathrm{m}$

correlation between I_θ and $\overline{w}$ is 0.41, similar to their correlation value for free convection conditions. The weak correlation is consistent with the much more fragmented spatial pattern of I_θ (Fig. 9a) than that of $\overline{w}$ (Fig. 8a). Interestingly, the imbalance is better correlated with the Reynolds vertical velocity variance $\overline{w'^2}$: the linear correlation coefficient is 0.55 at $u_g = 0\,\mathrm{m\,s^{-1}}$ and improves to 0.57 at $u_g = 4\,\mathrm{m\,s^{-1}}$.

Figure 10 presents the vertical profiles of the linear correlation (r) of $\overline{w}$ with $\overline{\theta}$, $\overline{\chi_b}$, and $\overline{\chi_t}$. The linear correlation is defined as

$$r = \frac{\langle \overline{w}\,\overline{\varphi} \rangle}{\left(\langle \overline{w}''^2 \rangle \langle \overline{\varphi}''^2 \rangle \right)^{\frac{1}{2}}} \tag{12}$$

where $\langle \overline{w}\,\overline{\varphi} \rangle$ is the spatial covariance between $\overline{w}$ and $\overline{\varphi}$, $\left(\langle \overline{w}''^2 \rangle \right)^{\frac{1}{2}}$ and $\left(\langle \overline{\varphi}''^2 \rangle \right)^{\frac{1}{2}}$ are the standard deviations of $\overline{w}$ and $\overline{\varphi}$, respectively.

Several broad features deserve attention. First, the effect of source location is evident. In the lower PBL ($z/z_i < 0.6$), $\overline{w}$ shows a much stronger correlation with heat and the

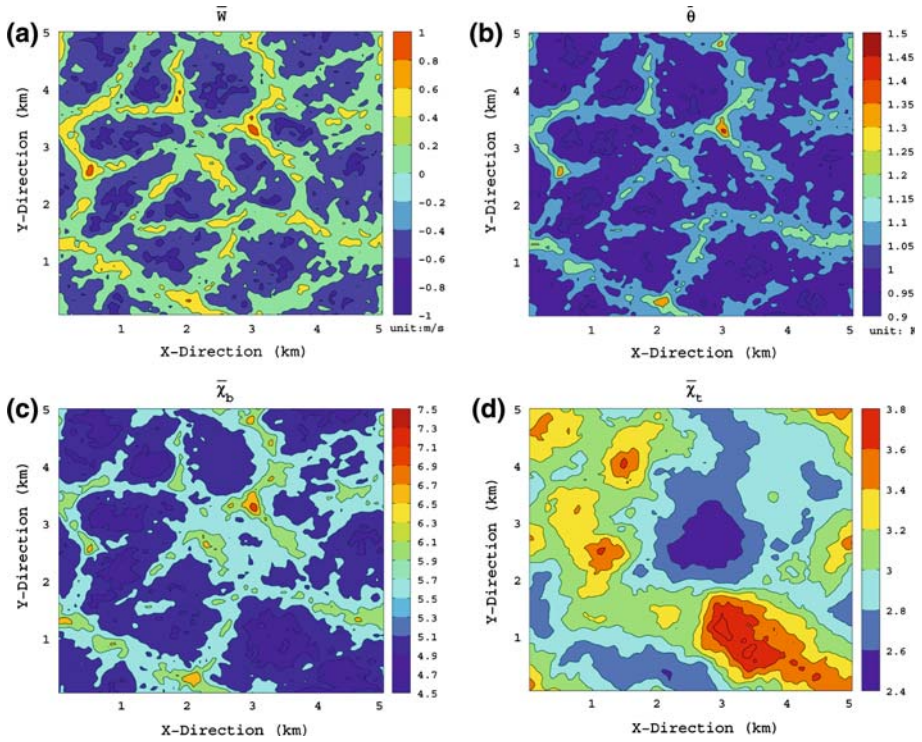

Fig. 8 Spatial distribution of Reynolds averaging (**a**) vertical velocity ($\overline{w}$), (**b**) potential temperature ($\overline{\theta}$), (**c**) the bottom–up tracer ($\overline{\chi_b}$), and (**d**) the top–down tracer ($\overline{\chi_t}$) for case B at $u_g = 0\,\mathrm{m\,s^{-1}}$. The averaging time period is $t_p = 1.8$ to 2.8 h, height $z = 100\,\mathrm{m}$

bottom–up tracer (linear correlation varies from 0.66 to 0.93 with mean values of 0.87 and 0.79 for $\overline{\theta}$ and $\overline{\chi_b}$, respectively) than with the top–down tracer (linear correlation ranges from 0.15 to 0.55 with a mean value of 0.40). Second, the surprisingly strong correlation between $\overline{w}$ and $\overline{\theta}$ or $\overline{\chi_b}$ exists in both free convection (Fig. 10a) and forced convection (Fig. 10b). In fact, for $\overline{\chi_b}$, the correlation coefficient is 0.85 at u_g of $4\,\mathrm{m\,s^{-1}}$, slightly larger than the value of 0.79 found at u_g of $0\,\mathrm{m\,s^{-1}}$. This is in contrast to the behaviour of the covariance $\langle \overline{w}\,\overline{\varphi} \rangle$, whose magnitude falls rapidly as u_g increases from 0 to $4\,\mathrm{m\,s^{-1}}$ (Fig. 7). Similar results are found when the model domain is enlarged to a size of $9.6\,\mathrm{km} \times 9.6\,\mathrm{km} \times 1.92\,\mathrm{km}$, indicating the correlation result is not an artifact of limited domain size. The spatial correlation between $\overline{w}$ and $\overline{\theta}$ is also comparable in magnitude to the linear correlation coefficient between the w and θ time series observed at a single point in the convective boundary layer.

Finally, we found that the change of covariance, $\langle \overline{w}\,\overline{\varphi} \rangle$ which exactly accounts for the flux imbalance, is closely associated with the standard deviation of $\overline{w}$ and $\overline{\varphi}$. As presented in Eq. 12, $\langle \overline{w}\,\overline{\varphi} \rangle$ is the product of r and these standard deviations. When u_g increases from 0 to $4\,\mathrm{m\,s^{-1}}$, the standard deviations decrease significantly even though r changes only slightly. Thus, PBL processes that lead to a reduction in the spatial variations of the time-averaged velocity and scalar concentration will improve the EC measurement.

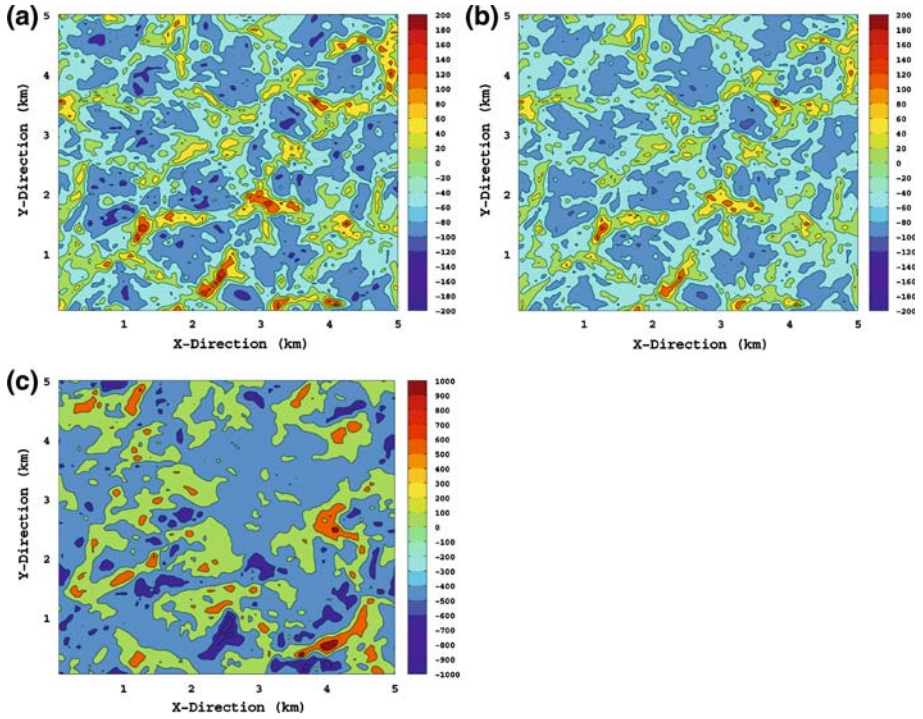

Fig. 9 Spatial distribution of flux imbalance of (**a**) heat, (**b**) the bottom–up tracer, and (**c**) the top–down tracer for the case B at $u_g = 0\,\mathrm{m\,s^{-1}}$. The averaging time period covers $t_p = 1.8$ to 2.8 h, height $z = 100\,\mathrm{m}$

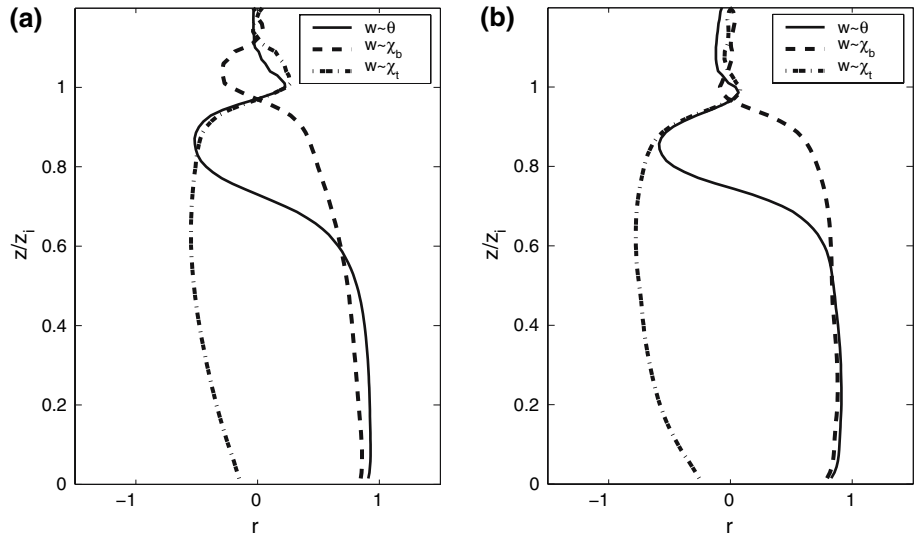

Fig. 10 Profiles of correlation coefficient (r) for vertical velocity (w) and potential temperature (θ),w and the bottom–up tracer (χ_b), as well as w and the top–down tracer (χ_t) at geostrophic winds of (**a**) $u_g = 0\,\mathrm{m\,s^{-1}}$, left panel and (**b**) $u_g = 4\,\mathrm{m\,s^{-1}}$, right panel (solid line: $w \sim \theta$, dash–line: $w \sim \chi_b$, dotted line: $w \sim \chi_t$)

5 Summary

The flux imbalance problem has been investigated with the NCAR's LES model. An online scheme has been implemented into the LES model to calculate Reynolds-averaged fluxes. A series of LES model simulations have been conducted to examine the dependence of flux imbalance on geostrophic wind, measurement height, surface heat flux, and entrainment. Our results are broadly consistent with previous studies on the flux imbalance problem, suggesting that previous results are robust and are not artefacts of numerical schemes.

A top–down (χ_t) and a bottom–up tracer (χ_b) have been incorporated into the LES model to investigate the impact of source location on the flux imbalance. The entrainment at the top of the PBL and thermal forcing at the surface have been found to have a profound influence on the flux imbalance in the convective PBL, especially in the free convection limit. In the lower part of the PBL, both heat and $\chi_b$show similar flux imbalance probability and spatial distribution patterns, indicating the heat flux imbalance is dominated by bottom–up diffusion. In the middle and upper parts of the PBL, the entrainment process plays an important role in the flux imbalance.

A set of non-dimensional functions have been presented to describe the dependence of the flux imbalance on key driving variables. The flux imbalance follows an exponential decreasing dependence on u_*/w_*, and an elliptic relationship with z/z_i. The non-dimensional velocity u_*/w_* is a good predictor of the flux imbalance for both the free and the forced convection regimes.

Acknowledgements This research was supported by the U.S. Department of Energy's Office of Science (BER) through the Northeastern Regional Center of the National Institute for Climatic Change Research. E.G. Patton would also like to acknowledge fruitful discussions with Harm Jonker (T.U. Delft, The Netherlands) regarding this work. This research used resources of the National Energy Research Scientific Computing Center, which is supported by the Office of Science of the U.S. Department of Energy.

References

Businger JA, Wyngaard JC, Izumi Y, Bradley EF (1971) Flux-profile relationships in the atmospheric surface layer. J Atmos Sci 28:181–189

Davis KJ, Bakwin PS, Yi C, Berger BW, Zhao C, Teclaw RM, Isebrands JG (2003) The annual cycles of CO_2 and H_2O exchange over a northern mixed forest as observed from a very tall tower. Global Change Biol 9:1278–1293

Deardorff JW (1980) Stratocumulus-capped mixed layers derived from a three-dimensional model. Boundary-Layer Meteorol 18:495–527

Jonker HJJ, Duynkerke PG, Cuijpers JWM (1999) Mesoscale fluctuations in scalars generated by boundary layer convection. J Atmos Sci 56:801–808

Kanda M, Inagaki A, Letzel MO, Raasch S, Watanabe T (2004) LES study of the energy imbalance problem with eddy covariance fluxes. Boundary-Layer Meteorol 110:381–404

Klemp JB, Durran DR (1983) An upper boundary condition permitting internal gravity wave radiation in numerical mesoscale models. Mon Wea Rev 111:430–444

Lee X (1998) On micrometeorological observations of surface-air exchange over tall vegetation. Agric For Meteorol 91:39–49

Lee X, Black TA (1993) Atmospheric turbulence within and above a Douglas-fir stand. Part 2: eddy fluxes of sensible heat and water vapor. BoundaryLayer Meteorol 64:369–390

Leuning R (2004) Measurements of trace gas fluxes in the atmosphere using eddy covariance: WPL corrections revisited. In: Lee X et al (eds) Handbook of micrometeorology: a guide for surface flux measurement and analysis. Kluwer Academic Publishers, Dordrecht pp 119–132

Mahrt L (1998) Flux sampling errors for aircraft and towers. J Atmos Oceanic Tech 15:416–429

Moeng CH (1984) A large-eddy simulation model for the study of planetary boundary-layer turbulence. J Atmos Sci 41:2052–2062

Patton EG, Sullivan PP, Moeng CH (2005) The influence of idealized heterologeneity on wet and dry planetary boundary layers coupled to the land surface. J Atmos Sci 62:2078–2097

Piacsek SA, Williams GP (1970) Conservation properties of convection difference schemes. J Comput Phys 6:392–405

Purnell DK (1976) Solution of the advective equation by upstream interpolation with cubic spline. Mon Wea Rev 104:42–48

Raasch S, Etling D (1998) Modeling deep ocean convection: large eddy simulation in comparison with laboratory experiments. J Phys Oceanogr 28:1786–1802

Raasch S, Schröter M (2001) PALM – a large eddy simulation model performing on massively parallel computers. Meteorol Z 10:363–372

Steinfeld G, Letzel MO, Raasch S, Kanda M, Inagaki A (2007) Spatial representativeness of single tower measurements and the imbalance problem with eddy-covariance fluxes: results of a large-eddy simulation study. Boundary-Layer Meteorol 123:77–98

Sullivan PP, McWilliams JC, Moeng CH (1996) A grid nesting method for large-eddy simulation of planetary boundary-layer flows. Boundary-Layer Meteorol 80:167–202

Twine TE, Kustas WP, Norman JM, Cook DR, Houser PR, Meyers TP, Prueger JH, Starks PJ, Wesely ML (2000) Correcting eddy-covariance flux underestimates over a grassland. Agric For Meteorol 103:279–300

Webb EK, Pearman GI, Leuning R (1980) Correction of flux measurements for density effects due to heat and water vapor transfer. Quart J Roy Meteorol Soc 106:85–100

Wilson K, Goldstein A, Falge E, Aubinet M, Baldocchi D, Berbigier P, Bernhofer C, Ceulemans R, Dolman H, Field C, Grelle A, Ibrom A, Law BE, Kowalski A, Meyers T, Moncrieff J, Monson R, Oechel W, Tenhunen J, Valentini R, Verma S (2002) Energy balance closure at FLUXNET sites. Agric For Meteorol 113:223–243

Wyngaard JC, Brost RA (1984) Top-down and bottom–up diffusion of a scalar in the convective boundary layer. J Atmos Sci 41:102–112